REPORT DOCUMENTATION PAGE

Form Approved
OMB NO. 0704-0188

Public Reporting burden for this collection of information is estimated to average 1 hour per response, including the time for reviewing instructions, searching existing data sources, gathering and maintaining the data needed, and completing and reviewing the collection of information. Send comment regarding this burden estimates or any other aspect of this collection of information, including suggestions for reducing this burden, to Washington Headquarters Services, Directorate for information Operations and Reports, 1215 Jefferson Davis Highway, Suite 1204, Arlington, VA 22202-4302, and to the Office of Management and Budget, Paperwork Reduction Project (0704-0188,) Washington, DC 20503.

1. AGENCY USE ONLY (Leave Blank)	2. REPORT DATE December 22, 2003	3. REPORT TYPE AND DATES COVERED Final 10/1/1999 – 9/30/2003

4. TITLE AND SUBTITLE Sub-1nm Patterning Accuracy via Spatial-Phase Locking	5. FUNDING NUMBERS DAAD19-99-1-0280

6. AUTHOR(S)

Prof. Henry I. Smith

7. PERFORMING ORGANIZATION NAME(S) AND ADDRESS(ES) Massachusetts Institute of Technology Research Laboratory of Electronics 77 Massachusetts Avenue Cambridge, MA 02139	8. PERFORMING ORGANIZATION REPORT NUMBER

9. SPONSORING / MONITORING AGENCY NAME(S) AND ADDRESS(ES) U. S. Army Research Office P.O. Box 12211 Research Triangle Park, NC 27709-2211	10. SPONSORING / MONITORING AGENCY REPORT NUMBER 40302-EL .3

11. SUPPLEMENTARY NOTES
   The views, opinions and/or findings contained in this report are those of the author(s) and should not be construed as an official Department of the Army position, policy or decision, unless so designated by other documentation.

12 a. DISTRIBUTION / AVAILABILITY STATEMENT Approved for public release; distribution unlimited.	12 b. DISTRIBUTION CODE

13. ABSTRACT (Maximum 200 words)

Scanning-electron-beam lithography (SEBL) is an essential tool for creating patterns of arbitrary geometry at feature sizes below 100 nm, even down to 15 nm dimensions. Aside from the slow writing speed, the most outstanding problem of SEBL is its inability to achieve pattern-placement accuracy that is compatible with its resolution. For example, commercial SEBL systems, costing several millions of dollars, can under the most ideal conditions achieve placement accuracy of about 20 nm. To solve this problem MIT invented and has pursued a novel approach called spatial-phase locking. The objective of this grant was to demonstrate the efficacy of spatial-phase-locked e-beam lithography (SPLEBL) in achieving 1-nm level placement accuracy. SPLEBL replaces the normally open-loop approach to scanning-electron-beam lithography (SEBL) with a closed-loop approach.

14. SUBJECT TERMS	15. NUMBER OF PAGES
	16. PRICE CODE

17. SECURITY CLASSIFICATION OR REPORT UNCLASSIFIED	18. SECURITY CLASSIFICATION ON THIS PAGE UNCLASSIFIED	19. SECURITY CLASSIFICATION OF ABSTRACT UNCLASSIFIED	20. LIMITATION OF ABSTRACT UL

NSN 7540-01-280-5500

Standard Form 298 (Rev.2-89)
Prescribed by ANSI Std. 239-18
298-102

20040112 009

Final Report on
Grant No. DAAD19-99-1-0280

October 1, 1999 – September 30, 2003

Sub-1nm Patterning Accuracy via Spatial-Phase Locking

Submitted by:

Professor Henry I. Smith
Massachusetts Institute of Technology
60 Vassar Street
Rm 39-427
Cambridge, MA 02139

December 19, 2003

Contents

1   Statement of the Problem Studied

Scanning-electron-beam lithography (SEBL) is an essential tool for creating patterns of arbitrary geometry at feature sizes below 100 nm, even down to 15 nm dimensions. Aside from the slow writing speed, the most outstanding problem of SEBL is its inability to achieve pattern-placement accuracy that is compatible with its resolution. For example, commercial SEBL systems, costing several millions of dollars, can under the most ideal conditions achieve placement accuracy of about 20 nm. To solve this problem MIT invented and has pursued a novel approach called spatial-phase locking. The objective of this grant was to demonstrate the efficacy of spatial-phase-locked e-beam lithography (SPLEBL) in achieving 1-nm level placement accuracy. SPLEBL replaces the normally open-loop approach to scanning-electron-beam lithography (SEBL) with a closed-loop approach.

2   Summary of the Most Important Results[a]

Several modes of SPLEBL were investigated, and several material configurations attempted. The "segmented-grid" mode proved effective, particularly in the fabrication of integrated optical circuits, but was limited by the time delay between registering the scan raster relative to the grid and completion of the writing. Environmental disturbances during the time delay limited the pattern-placement accuracy to standard deviations just under 3 nm. The "sparse-sampling" mode was limited by poor signal-to-noise ratio from the scintillating fiducial grid that was employed, and also by the inevitable time delay. This mode achieved pattern placement accuracy with standard deviation of 17 and 18 nm for X and Y respectively. The "continuous-feedback" or "real-time" mode, which provides the most comprehensive solution to pattern-placement accuracy, was implemented in a raster-scan mode on the Raith 150 SEBL system, and achieved pattern-placement accuracy of 1.2 nm, 1-sigma. This represents an improvement of about a factor of 30 over conventional approaches to e-beam lithography.

3   Pattern Placement in Scanning-Electron-Beam Lithography (SEBL)

Pattern placement is a general term that encompasses the accuracy, precision, and repeatability with which one can position a pattern element (i.e. a "feature") on a substrate. Pattern-placement accuracy is simply defined as the positional deviation of a pattern element relative to an ideal, mathematically defined, coordinate system. Pattern-placement precision is defined by the positional deviation from an accepted standard. Finally, pattern-placement repeatability is defined as the positional deviation observed from exposure-to-exposure on the same patterning system.

In conventional SEBL, pattern-placement precision is achieved by measuring the stage position with a laser interferometer. If the stage is not located in the correct position, one can deflect the beam, or use an additional, shorter-travel stage, to make fine corrections. This yields a precise measurement of the stage-mirror position with respect to a reference mirror, but there is no way to determine the position at which the beam strikes the sample.

---

[a]Most of the material in the body of this report was taken from the PhD thesis of J. Todd Hastings, MIT PhD June 2003.

This must be inferred from intermittent calibrations. Such calibrations correct only for long-term drift, not for the many other errors which influence pattern placement.

The time scale of a particular error determines how it will influence pattern placement. An error occuring on the time scale of the pixel-to-pixel beam motion (10 ns to 1 μs), for example instability in the least-significant bit (LSB) of a digital-to-analog converter (DAC), may not shift the centroid of a feature, but may appear as line edge roughness. Errors with longer characteristic times, such as mechanical vibration, may influence pattern placement between subsequently exposed features. Errors with very long time scales, such as thermal expansion or contraction, may introduce gradual errors spanning large areas of the substrate. Finally, some errors, such as distortions due to substrate mounting, are quasi-static. These errors change only from exposure-to-exposure. Figure 1 assigns various sources of error to a corresponding time scale.

Time Scale (seconds)	10^{-6}	10^{-2}	10^1	10^4	
	Pixel to Pixel	Feature to Feature	Field to Field	Exposure to Exposure	Quasi-static
	DAC quantization	charging			deflection non-linearity
		vibration	sympathetic beam/stage motion	field calibration	electron-optics distortions
		stray EM fields			
		interferometer quantization	thermal gradiants and variations	substrate mounting distortion	interferometer mirror errors
		deflection hysteresis			stage calibration

Figure 1: SEBL pattern-placement errors arise from a number of sources which affect the pattern differently depending on their time-scale. The slowest time scales (right) impact global placement accuracy, while shorter time scales (left) adversely affect placement from feature to feature.

SEBL builds up a pattern from a set of stitched fields or stripes, and errors occuring at the field or stripe boundaries are termed stitching errors. These errors are highly visible because features exhibit discrete offsets or breaks at the boundary. Figure 2 illustrates typical stitching errors. When examining stitching errors one usually observes both a deterministic and a stochastic component. The deterministic part, or mean stitching error, arises from factors including miscalibration of the deflection system, uncorrected distortion in the deflection field, or drift of the beam or stage. The stochastic component usually arises from inaccuracy in stage-positioning, system or substrate charging, vibrations, or interferometer quantization.

Pattern placement accuracy has been a serious problem in SEBL and in projection e-beam lithography as well. The MEBES 5500 SEBL system, manufactured by ETEC,
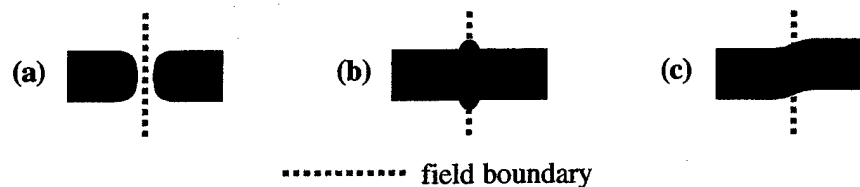
Figure 2: Stitching errors occur at field and stripe boundaries. The resulting pattern can exhibit **(a)** breaks from incomplete exposure, **(b)** bulges from overlapped exposures, and/or **(c)** discrete offsets.

specified 30 nm maximum placement errors. JEOL specifies 30 nm placement accuracy for its JBX-9000 MV mask writer. NuFlare Technology claims 12 nm 3-sigma positioning accuracy for its new EBM-4000 shaped-beam tool. NTT developed an e-beam writer, EB-X3, for x-ray mask writing and published data showing sub-15nm placement accuracy. In evaluation these specifications, one must bear in mind that these values are obtained only in highly controlled environments that are free of electromagnetic disturbances, vibrations, and other effect that would degrade performance. In fact, the facilitation that is needed for e-beam systems to achieve the stated specifications adds greatly to the cost of e-beam lithography. Spatial-phase locking is intended to achieve nanometer-level pattern placement accuracy but without the extreme care and expensive facilitation that is required in conventional SEBL to achieve only 15 nm placement accuracy.

4 Spatial-Phase-Locked Electron-Beam Lithography (SPLEBL)

Spatial-phase-locked electron-beam lithography (SPLEBL), shown schematically in Fig. 3, provides feedback control for precise beam positioning. By monitoring the phase of the periodic signal produced by the fiducial grid, one can ascertain the position of the e-beam on the substrate. As a result, SPLEBL provides inherent pattern placement precision and repeatability, but the absolute pattern-placement accuracy depends on the accuracy of the grid itself.

The fiducial grid is a key component of SPLEBL. Since pattern placement is tied to the grid absolute accuracy, can be no better than the fidelity of the grid. Thus, the grid should have spatial-phase coherence over an area at least as large as the substrate to be written in the e-beam system, and a known value of spatial frequency. At MIT a number of techniques have been developed to ensure spatial-phase fidelity in grids for SPLEBL [theses, marks]. In this report we take for granted that the grid has fidelity compatible with 1 nm placement accuracy.

Several approaches to spatial-phase locking have been implemented and are categorized by whether they provide continuous or discontinuous feedback. Discontinuous feedback modes, often described as "look-then-write" modes, scan the beam over the grid before exposing each field. After correcting the beam deflection, the pattern is written normally. In the segmented-grid implementation of SPLEBL, the fiducial grid is segmented to small, unused portions of each field. This technique sacrifices substrate area for the grid, but one can use strongly scattering materials (i.e. heavy metals) and one can examine the grid at high doses. These advantages yield high signal-to-noise ratios (SNR), and, as a
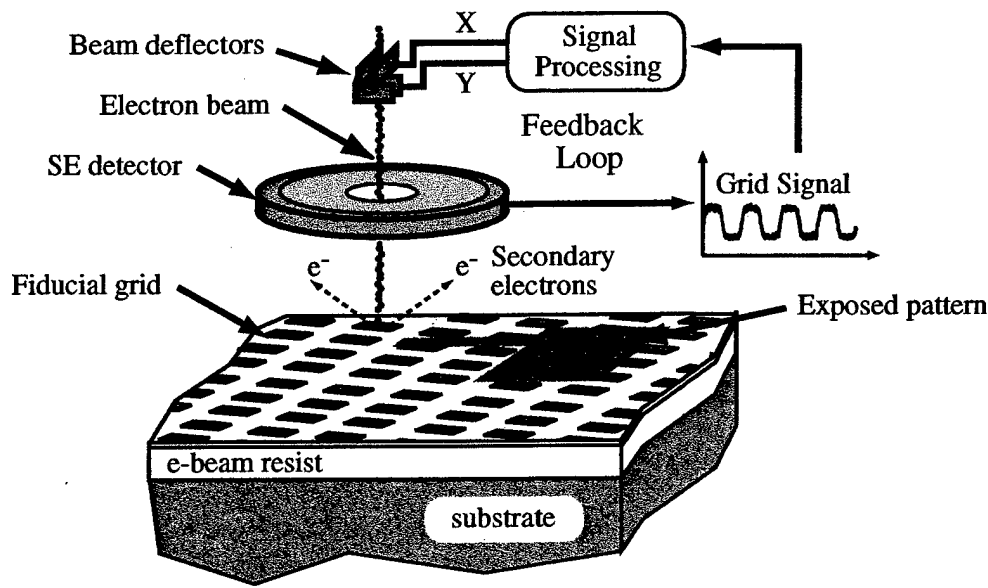
Figure 3: Spatial-phase-locked e-beam lithography provides feedback control for accurate pattern placement by monitoring the signal produced by a fiducial grid on the substrate. Because the grid signal is periodic, one can use phase detection to locate the beam within a small fraction of one period.

result, precise phase locking. A variety of integrated optical devices were patterned using segmented-grid spatial-phase locking.

Another discontinuous feedback approach relies on sparsely sampling the fiducial grid using an array of point exposure. These samples cover the entire field to be written, but they are taken at sub-exposure-threshold doses. Typically the sample spacing is larger than the grid period, and one detects an aliased signal, or moiré pattern. In the sparse-sampling mode of SPLEBL, the grid covers the entire substrate and must not perturb the electron beam. As a result, it is difficult to obtain high SNRs using this technique, but no substrate area is sacrificed.

In the continuous feedback mode of SPLEBL, the system constantly monitors the signal from a global grid as the beam scans across the substrate. This technique is most naturally implemented with raster-scan exposure strategies. Ideally, when the system addresses areas of the pattern that are not to be exposed, a reduced-current beam would allow the grid signal to be monitored without exposing the resist. In exposed areas the beam would remain at full current. While the discontinuous feedback modes correct for stage errors and slow beam drift, continuous feedback corrects for more rapid variations. No substrate area is required, and continuous sampling makes low SNRs more tolerable.
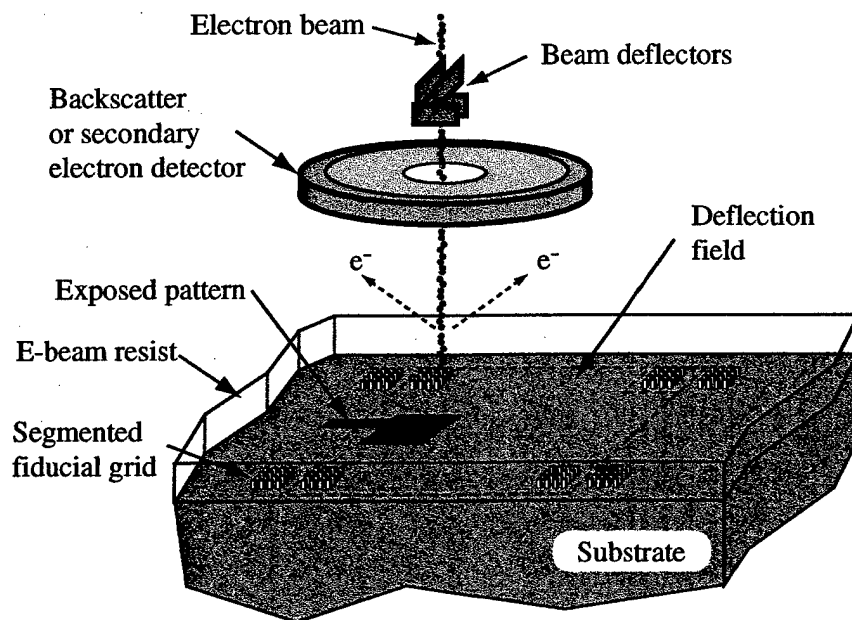
Figure 4: In segmented-grid spatial-phase locking, the e-beam scans over the grid in isolated areas. After measuring the spatial-phase in these regions, the beam deflection is corrected, and the pattern is exposed normally.

5 Results of Discontinuous Feedback SPLEBL

5.1 The Segmented Grid Mode

The segmented grid mode of SPLEBL is depicted in Fig. 5.1. A variety of experiments in the segmented-grid mode were carried out on the Raith 150 SEBL system. Figure 5 shows placement-error histograms for this mode, taken at several positions over an 88 μm wide scan field. The technique used to measure the errors is described in reference [??]. The important conclusion is that a standard deviation under 3 nm is achieved in this mode. This is about an order of magnitude improvement over what is achievable in a conventional commercial SEBL system. So this simple mode of SPLEBL, which can be easily implemented in any e-beam system in the world, is capable of significantly improving placement accuracy over what is available in a conventionally operated system. Nevertheless, this mode is useful only for a limited set of applications; in particular it would not be applicable to the highly dense patterns of a microprocessor or memory chip. One very important application is integrated optical devices which often require long-range spatial-phase coherence. Such work is described in several of the technical articles published as a result of this research.

5.2 The Sparse Sampling Mode

In the sparse-sampling mode of SPLEBL a global-fiducial grid is sampled at discrete locations within the e-beam field with a sub-exposure dose. Like the segmented-grid mode, beam positioning feedback is only supplied before exposing each field. Unlike the segmented grid mode, the sparse-sampling mode uses a global grid that does not occupy valuable sub-
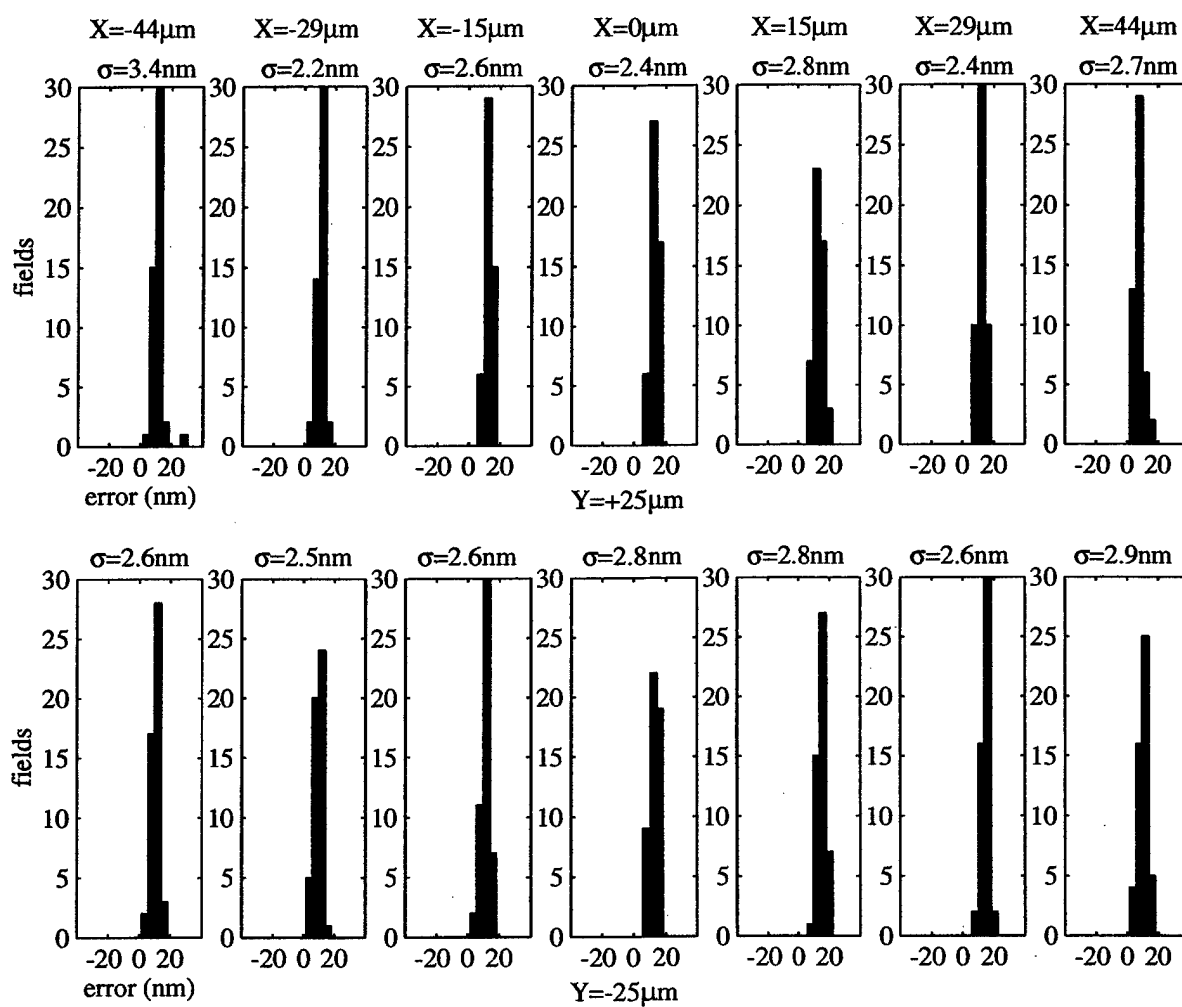
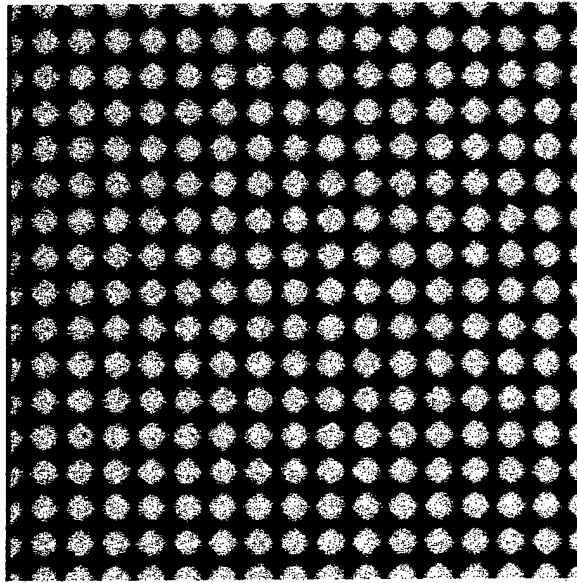Figure 5: Segmented grid SPLEBL placement error histograms.

Figure 6: Moiré pattern formed by a 512×512 sample array of a 1-μm-period grid over a 528 μm field. Image was acquired using backscattered electrons from a Au grid on silicon.

strate area. The sparse sampling mode was implemented on MIT's VS2A SEBL system, and tested with both metallic and scintillating fiducial grids.

In practice, sparse samples are taken at spacings larger than the grid period. Because the spatial frequency of the fiducial grid is greater than the spatial frequency of the sparse samples, the acquired signal will be aliased. In the spatial domain, aliased periodic signals appear as moiré patterns. Figure 5.2 shows the moiré pattern formed by sampling a 1μm-period gold grid at 512×512 equally spaced points within a 528μm field. The number of periods in the moiré is simply given by the difference between the number of sample points and the number of fiducial grid periods in a given direction, in this case exactly 16 periods in both X and Y.

Moiré patterns provide a sensitive tool for measuring deflection-field alignment and distortion. The spatial phase of the moiré signal represents the spatial phase of the periodic sample locations with respect to the underlying fiducial grid. Thus, the deflection field can be shifted into alignment with the fiducial grid by locking the spatial phase of the moiré pattern to a specified value. Moiré patterns also reveal deflection distortions. Variation of the moiré phase with position in X or Y indicates a rotation, or skew, of the deflection field with respect to the grid. If this variation differs between X and Y the deflection axes are not orthogonal. The spatial frequency of the moiré pattern allows one to precisely calculate the scale (magnification) of the field. Finally, a linear variation of X-spatial frequency with Y, or vice-verse, indicates the presence of trapezoidal distortion.

The VS2A SEBL system uses eight parameters to model and correct the error between desired beam position (x_P, y_P) and actual beam position (x_B, y_B). These relationships are

given by

$$x_B = a_0 + a_1 x_P + a_2 y_P + a_3 x_P y_P \qquad (1)$$

$$y_B = b_0 + b_1 x_P + b_2 y_P + a_3 x_P y_P \qquad (2)$$

where the coefficients a_0, a_1, a_2, and a_3 represent the shift, scale, rotation (skew), and trapezoidal distortion errors for the x-axis, respectively. Figure 7 shows moiré patterns corresponding to various distortions.
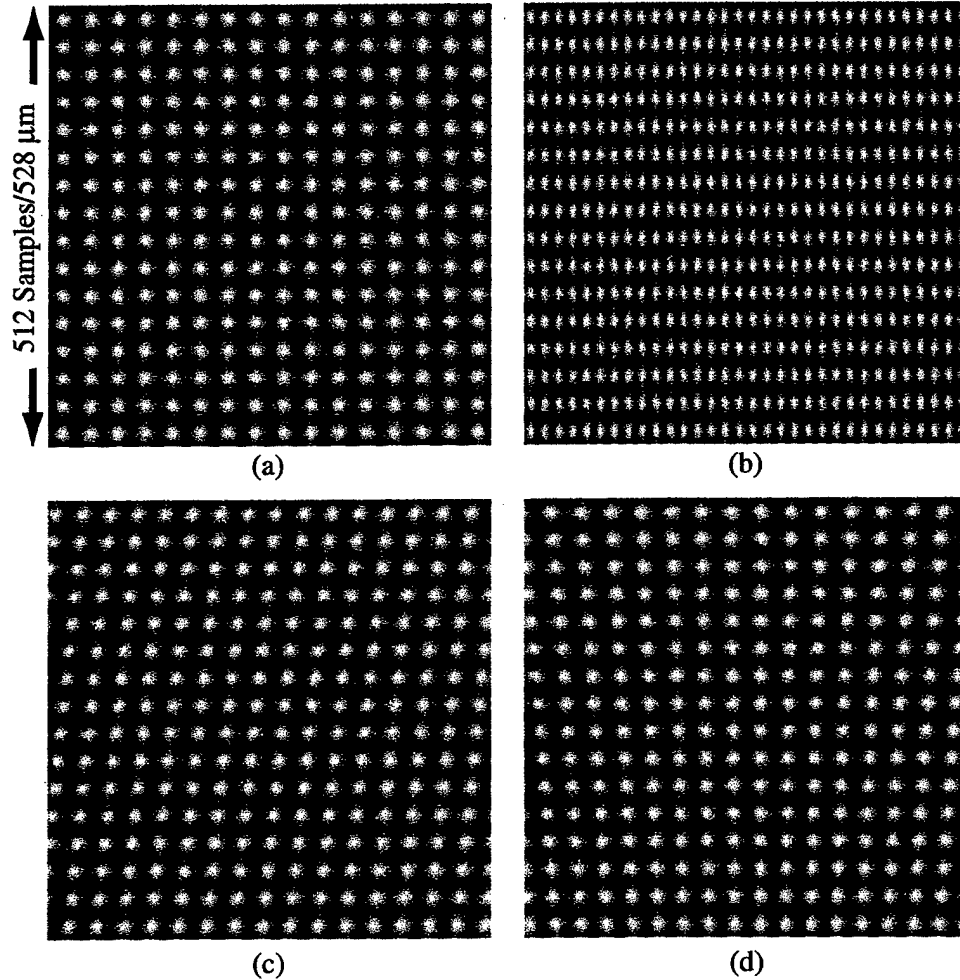

Figure 7: Moiré patterns formed by a 512×512 samples of 1-μm-period grid over a 528 μm field with various deflection errors. (a) Perfect deflection. (b) X-deflection scaled: $a_1 = 1.03$. (c) X-deflection skewed: $a_2 = 0.003$ radians. (d) Trapezoidal distortion along the y-direction: $a_3 = 1 \times 10^{-5}$.

In any practical implementation of the sparse-sampling mode, the global fiducial grid must be non perturbative, that is, it must not impede or interfere with the SEBL patterning. We chose to develop and use a scintillating fiducial grid for this purpose. The signal from the grid was detected by a photomultiplier. Although we obtained results with the
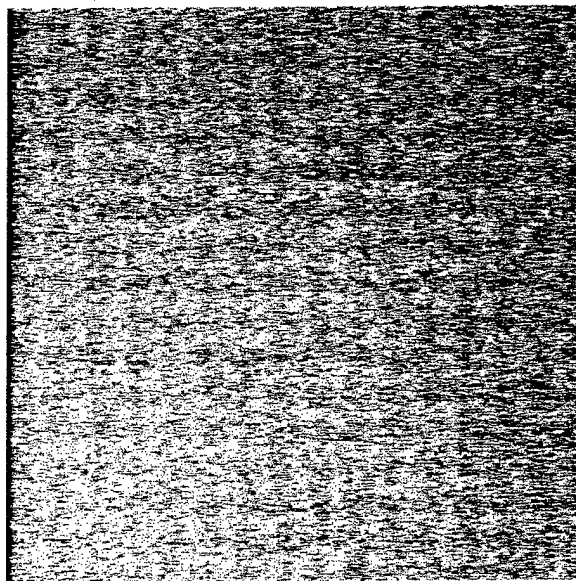
Figure 8: Moiré patterned formed by 512 × 512 samples of a 530-μm scintillating grid over a 280 μm field. The scintillating layer (PMMA, anthracene, naphthalene, and POPOP) served as a the e-beam resist and the fiducial grid.

scintillating grid, we eventually concluded that the signal-to-noise was too low to enable high performance SPLEBL and eventually dropped this line of investigation.

Figure 8 illustrates the high-noise signal obtained from a scintillating fiducial grid, and Figure 9 shows histograms of the stitching errors obtained with the sparse sampling mode. Although we recognized several avenues for improving the results of the sparse sampling mode, we opted instead to focus our efforts on the continuous feedback mode of SPLEBL.

6 The Continuous-Feedback Mode of SPLEBL

To implement the continuous feedback mode of SPLEBL (also called "real time" SPLEBL) on the Raith 150 SEBL system, we modified the Raith to enable raster scanning. Normally the Raith is configured for vector scanning.

As the e-beam raster-scans across the field, the grid produces a continuous signal. If the grid is aligned to the deflection axes, and the beam scans rapidly along the x-axis, we will have to acquire a number of lines of data to detect any y-deflection error. To correct for shift along both axes simultaneously, it is necessary to rotate the grid with respect to the field. With a rotated grid, one can estimate the beam shift for each axis, pass this signal through an appropriate filter, and feedback corrections to the deflection system. We implemented this strategy in the Raith 150 system by adding a dedicated microprocessor running a real-time, deterministic operating system and high-speed analog-to-digital and digital-to-analog conversion. Processing the signal in the digital domain allowed the bulk of the phase-locking and distortion-correction systems to be implemented and revised in software.
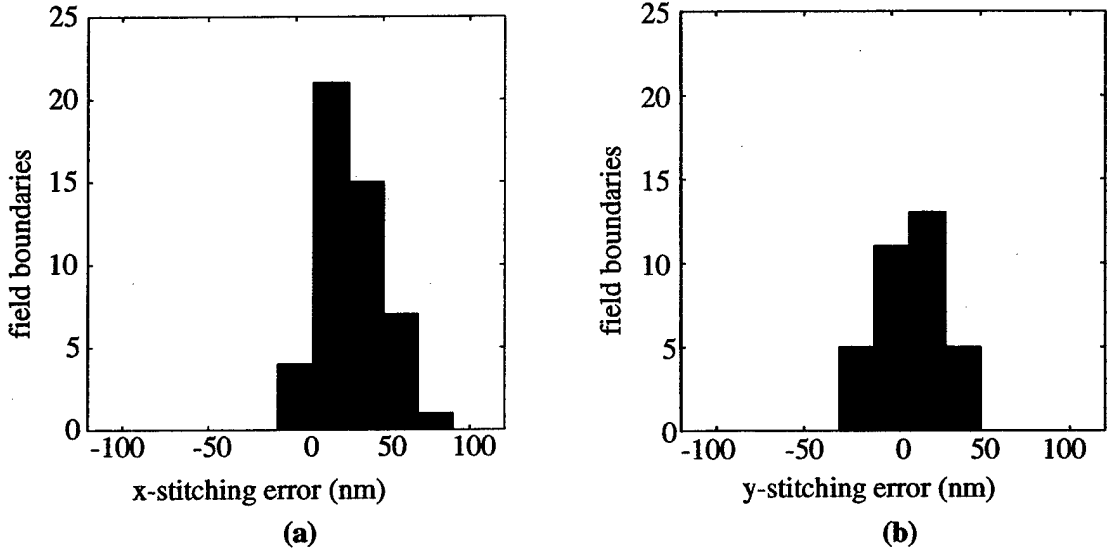
Figure 9: Histograms for x (a) and y (b) stitching errors obtained with a 530-nm-period scintillating grid and sparse-sampled SPLEBL. The standard deviations for x and y are 17 nm and 18 nm, respectively.

6.1 Beam-Shift Extraction from the Grid Signal

To provide continuous feedback control we must first extract the beam-placement error from the fiducial grid signal. We define the following coordinate system: x_P and y_P are the intended e-beam coordinates produced by the digital pattern generator. x_B and y_B are the real coordinates of the electron beam. For real-time spatial-phase locking, we are only interested in the beam shift, other deflection errors are dealt with separately, as described before. Thus, the real and intended coordinates are simply related by

$$x_B = x_P + \Delta x \tag{3}$$

$$y_B = y_P + \Delta y \tag{4}$$

To correct deflection along both axes, we wish to lock the beam position to a grid with period Λ_G that is rotated by some angle θ with respect to the scan direction. Figure 10 shows an SEM image of the fiducial grid rotated with respect to the scan axes. The x-axis is the fast deflection axis and the direction along which we perform phase-detection. If we assume a purely sinusoidal grid signal, we can model it as

$$S(x_B, y_B) = a \cos \left[k_0 \left(x_B \cos \theta + y_B \sin \theta \right) \right] + a \cos \left[k_0 \left(y_B \cos \theta - x_B \sin \theta \right) \right] \tag{5}$$

where the grid's spatial-frequency is given by $k_0 = 2\pi/\Lambda_G$.

If we substitute equations 3 and 4 into equation 5 and take the Fourier transform with respect to x_P we find that

$$
F_x(k, y_P) = \frac{a}{2} \delta \left(k \pm k_0 \cos \theta \right) \exp \left[\pm j k_0 \left(\Delta x \cos \theta + \Delta y \sin \theta + y_P \sin \theta \right) \right]
$$
$$
+ \frac{a}{2} \delta \left(k \pm k_0 \sin \theta \right) \exp \left[\mp j k_0 \left(-\Delta x \sin \theta + \Delta y \cos \theta + y_P \cos \theta \right) \right].
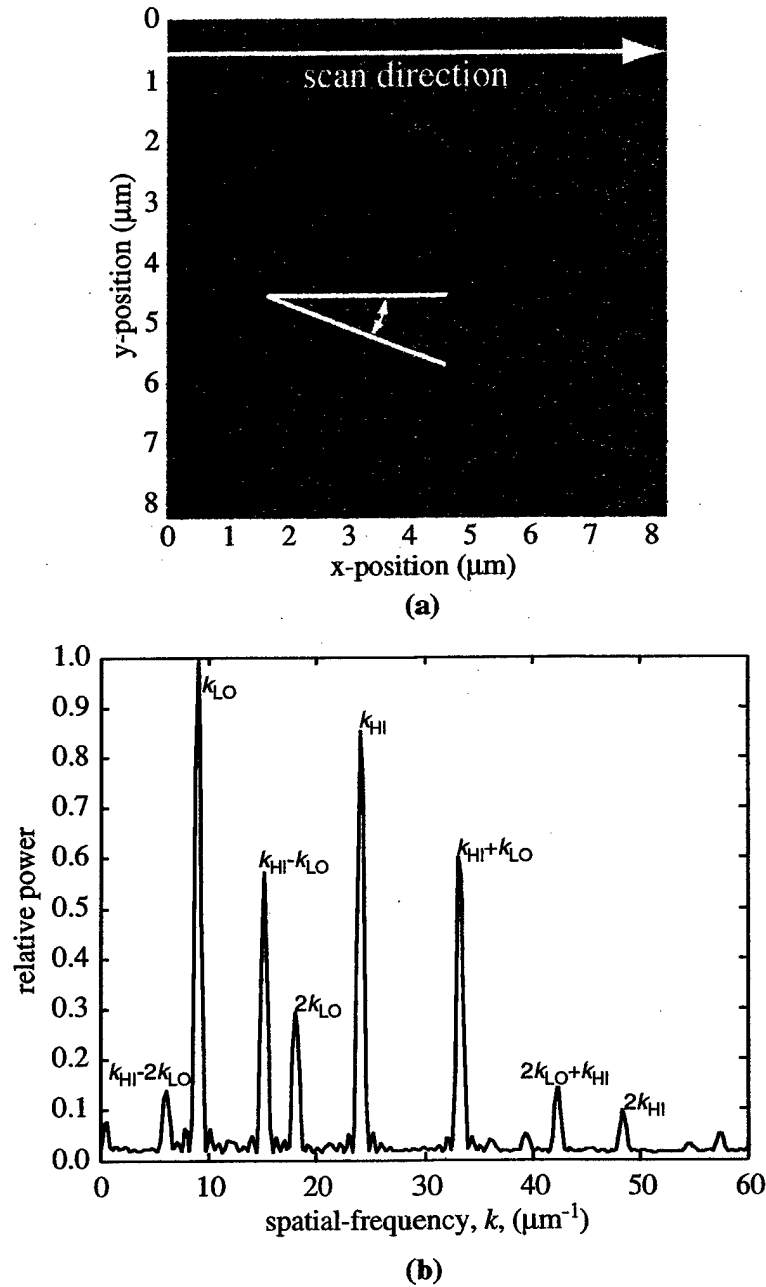$$

(a)

(b)

Figure 10: For 2D, real-time spatial-phase locking we scan
the beam at an angle, θ, with respect to the grid axes. **(a)**
shows a secondary electron image of a 246-nm period Al grid
on SiO_2 on PMMA. The averaged spatial-frequency spectrum
is shown in **(b)** where fundamental, harmonic, and sum and
difference frequency components are labeled.

We obtain two positive spatial-frequency components: $k_{\mathrm{HI}} = k_0 \cos\theta$ and $k_{\mathrm{LO}} = k_0 \sin\theta$. The phases, ϕ_{HI} and ϕ_{LO}, for these two frequencies are given by

$$\phi_{\mathrm{HI}} = k_0 \left(\Delta_x \cos\theta + \Delta_y \sin\theta + y_P \sin\theta \right), \text{ and} \tag{6}$$

$$\phi_{\mathrm{LO}} = -k_0 \left(-\Delta_x \sin\theta + \Delta_y \cos\theta + y_P \cos\theta \right). \tag{7}$$

The last term in each of the above equations is determined by θ and y_P, both of which are known for any given measurement. This last term leads to a deterministic phase progression in ϕ_{HI} and ϕ_{LO} as the beam progresses in the y direction. Thus, we can subtract this phase offset and measure only the phase-error terms, $\Delta\phi_{\mathrm{HI}}$ and $\Delta\phi_{\mathrm{LO}}$, given by

$$\Delta\phi_{\mathrm{HI}} = k_0 \left(\Delta_x \cos\theta + \Delta_y \sin\theta \right), \text{ and} \tag{8}$$

$$\Delta\phi_{\mathrm{LO}} = -k_0 \left(-\Delta_x \sin\theta + \Delta_y \cos\theta \right). \tag{9}$$

We calculate the x- and y- shift by solving these equations for Δx and Δy.

$$\Delta x = \frac{1}{k_0} \left(\Delta\phi_{HI} \cos\theta + \Delta\phi_{LO} \sin\theta \right), \text{ and} \tag{10}$$

$$\Delta y = \frac{1}{k_0} \left(\Delta\phi_{HI} \sin\theta - \Delta\phi_{LO} \cos\theta \right). \tag{11}$$

It is possible to extend this technique to calculate scaling, rotation, and higher-order distortions in real time. After estimating k_{LO}, k_{HI}, ϕ_{LO}, ϕ_{HI}, and their first derivatives with respect to y_P, one can correct shift, scaling, and rotation for each axis in real-time. This was deemed unnecessary because these errors are relatively stable during a single exposure. In addition, one can monitor these errors, and higher-order distortions, from field-to-field using the technique described before.

It may appear that locking to a rotated grid provides better phase-locking precision for one axis than the other. Fortunately, this is not the case. If one samples several periods for each spatial-frequency, and satisfies the Nyquist criterion, the variance of the phase estimate depends only on the SNR and the number of samples. Therefore,

$$\sigma^2_{\phi_{\mathrm{HI}}} = \sigma^2_{\phi_{\mathrm{LO}}} = \sigma^2_\phi \approx \frac{2}{\gamma N} \tag{12}$$

where γ is the signal-to-noise ratio and N is the number of samples. If we calculate the variance of Δx and Δy based on equations 10 and 11, we find that

$$\sigma^2_{\Delta x} = \sigma^2_{\Delta y} = \frac{\sigma^2_\phi \left(\cos^2\theta + \sin^2\theta \right)}{k_0^2} = \frac{\sigma^2_\phi}{k_0^2} \tag{13}$$

While most rotation angles provide good phase-locking, one must remember that k_{LO} approaches zero for small angles and the discrete Fourier-transform is no-longer an efficient estimator. As θ approaches 45° both k_{LO} and k_{HI} approach $\sqrt{2}k_0/2$ and cause interference between the phase estimates. Finally, signals from metallic grids also contain harmonics and sum and difference frequencies of k_{HI} and k_{LO}, as seen in figure 10(b). Overlap between these spurious frequencies and the fundamental frequencies causes additional phase estimation errors.

12

6.2 Feedback Control Loop

SPLEBL provides closed-loop control for e-beam lithography by detecting the beam position and feeding back corrections to the deflection system. This process can be represented by the system shown in Fig. 11. The control loops for the x- and y- axes are decoupled as long as we can estimate the phase of the low- and high-frequency components independently. If the frequency separation is large enough, and care is taken with the location of spurious frequencies, this is an appropriate assumption.

Figure 11(a) shows the decoupled x-axis loop which consists of the position input from the pattern generator, X_P, the EBL system, H_S, the placement-error estimation process, H_E, physical disturbances, D_{p1} and D_{p2}, and errors in the phase-estimation process, D_e. The physical disturbances are divided between those occuring in the electronics before the SEBL system input, D_{p1}, and those occuring between the beam deflection and the sample, D_{p2}. We wish to correct the physical errors without introducing excessive noise from the estimation errors. The subtraction of X_P from X_B is necessary because only the beam placement error is being fed back, not the beam position itself.

Before analyzing the system, we make two helpful simplifications shown in Fig. 11(b). First, we assume that large deflection errors have been removed with field calibration, and that the SEBL system function is ≈ 1 for the small amplitude, low frequency corrections of interest. As a result, we combine the two physical disturbances into a single term, D_p. Secondly, the estimation function is a simple average over the number of samples used for the DFTs. Thus, we can move the estimation error input before the estimator sub-system in the feedback path, and increase its magnitude by $\sqrt{N}$, where N is the number of samples. This simplification decouples the impact of signal-to-noise ratio and number of samples on the error estimate. Thus, the final analysis reveals the impact of increasing or decreasing the number of samples for a constant signal-to-noise ratio.

It remains to quantify the other system functions in figure 11(b). We have implemented a discrete-time feedback system, so we will work in the z-transform domain. The phase estimates are performed over a number of samples N; therefore, $\Delta \bar{x}(n)$ represents the average beam displacement from sample $n - N$ to sample n. Thus,

$$\Delta \bar{x}(n) = \frac{1}{N} \sum_{m=n-N+1}^{n} \Delta x(m), \text{ and} \tag{14}$$

$$H_E(z) = \frac{1}{N} \left[\frac{1 - z^{-N}}{1 - z^{-1}} \right]. \tag{15}$$

We describe the loop filter by its transfer function, H_F. We define transfer function coefficients, p and q, for the numerator and denominator respectively, and obtain

$$H_F(z) = \frac{p_1 + p_2 \, z^{-1} + p_3 \, z^{-2} + \cdots}{q_1 + q_2 \, z^{-1} + q_3 \, z^{-2} + \cdots}. \tag{16}$$

This form of the transfer function is implemented in a digital filter using the following algorithm.

$$q_1 \delta x(n) = p_1 \Delta x(n) + p_2 \Delta x(n - 1) + p_3 \Delta x(n - 2) + \cdots$$
$$- q_2 \, \delta x(n - 1) - q_3 \, \delta x(n - 2) - \cdots \tag{17}$$

where $\Delta x(n)$ is the nth beam-error estimate and $\delta x(n)$ is the nth filtered output for feedback correction.
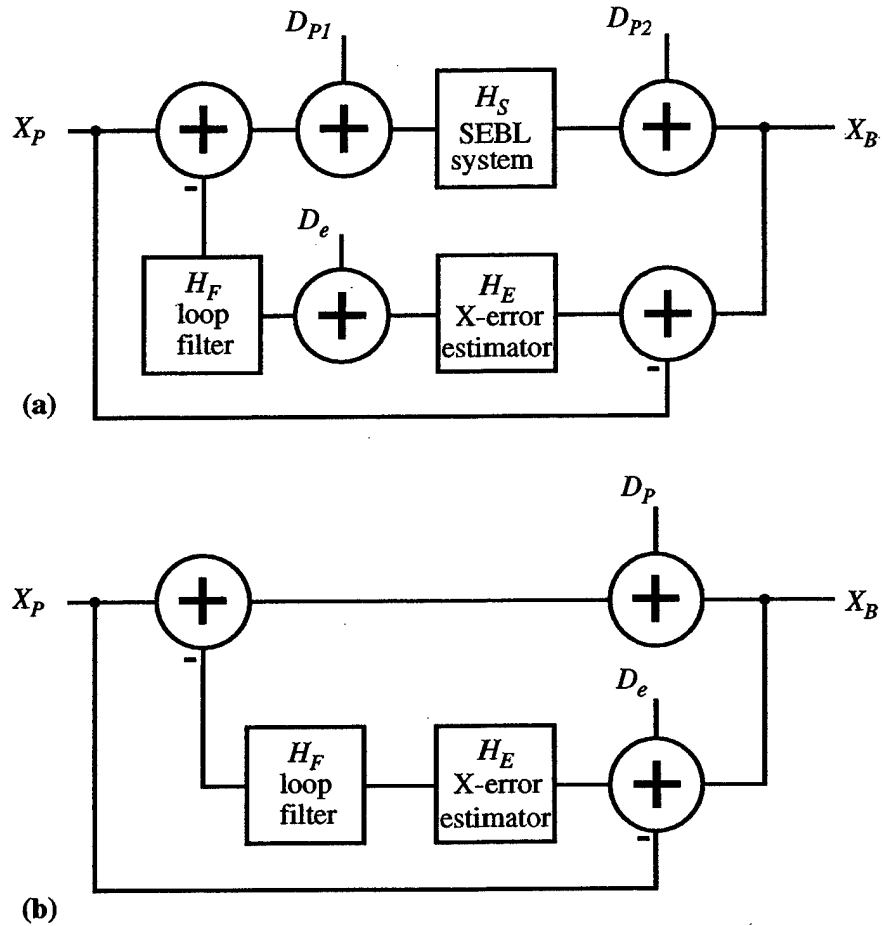
13

Figure 11: (a) Full control loop for the x-axis. The ideal beam position is given by X_P and the real beam position by X_B. D_{p1} and D_{p2} represent physical disturbances while D_e represents estimation errors. (b) Simplified x-axis control loop. The SEBL system transfer function is assumed to be 1, and the physical disturbances are combined in a single term, D_p.
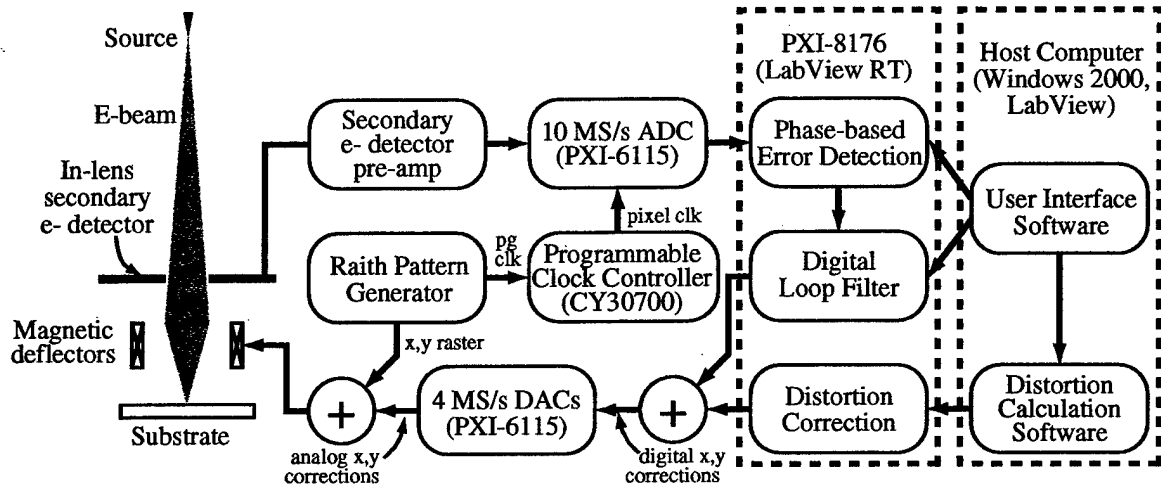
14

Figure 12: Schematic of the real-time spatial-phase locking system.

Combining the estimator and loop-filter responses with the disturbance functions, the beam-placement error, is given by

$$X_B - X_P = D_e \frac{H_E H_F}{1 + H_E H_F} - D_p \frac{1}{1 + H_E H_F} \qquad (18)$$

in the z-transform domain. Equation 18 reveals trade-offs in loop-filter design. For frequencies where $|H_F|$ becomes large $(X_B - X_P) \rightarrow D_e$; thus, estimation errors couple directly to the beam deflection. For frequencies where $|H_F|$ becomes small $(X_B - X_P) \rightarrow D_p$, and physical disturbances are not compensated. As a result, an intermediate filter response must be chosen such that one compensates for real disturbances without introducing errors from the phase-estimation process. Experimental details for the estimator and filter are given before.

6.3   Implementation on the Raith 150 System

To implement real-time spatial-phase locking, we combined a multi-function analog input-output board (model PXI-6115) with a dedicated Pentium III, 1.26 GHz microprocessor (model PXI-8714) in a PXI[b] chassis (model PXI-1000B) all supplied by National Instruments. The general purpose microprocessor and interface bus provide a flexible platform on which to developed spatial-phase locking. The phase-locking and distortion-correction algorithms reside entirely in software, allowing rapid testing and revision. Figure 12 shows a schematic of the real-time spatial-phase locking system. The following section discusses each component in detail.

To date, all real-time phase-locking experiments conducted with the Raith 150 system have used metallic grids and secondary electron detection. Thus, the signal from the in-lens secondary electron detector is routed to a 10 MHz analog-to-digital converter (ADC) on

---

[b]PXI (PCI eXtensions for Instrumentation) is an enhanced version of the compact-PCI (Peripheral Component Interconnect) standard, which itself is an industrial version of the standard PCI bus found in personal computers.

the National Instrument PXI-6115 data acquisition card. A 500 kHz, 3rd order, analog low-pass filter prevents aliasing in conversion.

The pixel clock derived from the pattern generator triggers the ADC to sample the secondary electron signal at each location the e-beam addresses. Thus, one converts from spatial to temporal frequency by multiplying by the beam-deflection velocity, v_B.

$$\omega_{\mathrm{HI}} = k_{\mathrm{HI}} v_B \tag{19}$$

$$\omega_{\mathrm{LO}} = k_{\mathrm{LO}} v_B \tag{20}$$

After the data acquisition board stores the desired number of samples, the data is transferred over the PCI bus (133 MB/sec maximum bandwidth) to the Pentium processor. This processor runs National Instrument's LabView Real-Time operating system. Real-time operating systems allow deterministic system control and require few memory or processor resources. As a result, critical control algorithms run reliably and consistently. Real-time systems generally do not provide user input or video output, so the software is developed on a standard PC and downloaded to the real-time system over Ethernet. User settings and data are also passed between the real-time processor and the Raith control computer over Ethernet.

Once the sampled grid signal reaches the processor, we estimate x- and y- placement error by calculating the DFT at k_{LO} and k_{HI}. For each value of y_P, corresponding to each scanned line, we phase shift the Fourier transform kernels, $e^{-jk_{\mathrm{LO}}x_n}$ and $e^{-jk_{\mathrm{HI}}x_n}$, by $y_P \cos\theta$ and $y_P \sin\theta$ respectively. Thus, we calculate only the phase errors, $\Delta\phi_{\mathrm{LO}}$ and $\Delta\phi_{\mathrm{HI}}$, and obtain the beam shifts, Δx and Δy, from equations 10 and 11. One could also calculate the phases with the standard Fourier transform kernel and then subtract the phase-offsets, but this approach introduces wrapping errors when the phases and phase-offsets approach $\pm\pi$.

We verified the performance of the phase-detection system using the 246-nm period aluminum fiducial grid described below. The grid was rotated -0.352990 radians with respect to the deflection axes, and sampled at a variety of signal-to-noise ratios. We adjusted the SNR by varying the beam current and beam energy. The real-time system only stores phase- and amplitude estimates for each block of 1000 samples, not the signal level for every sample of the grid. As a result, we estimate the SNR by finding the mean and variance of the two fundamental frequency amplitudes, a. For high SNR, $\mathrm{var}(a) = 2\sigma^2/N$; thus, the SNR is given by $\gamma = 2\bar{a}/(N\,\mathrm{var}(a))$. This is a biased estimator, but we can reasonably correct for the bias down to $\gamma \approx 0.01$. We compare the SNR and variance of the phase-estimate over a small region (10 μm $\times$ 10 μm) where we assume the mean phase is constant. Figure 13 plots this comparison in terms of beam shift. One can see that the standard deviation of the shift-estimate tracks the Cramer-Rao bound, so we remain in the noise limited regime. We need to filter the feedback signal to compensate for real disturbances without introducing additional errors from phase-estimation uncertainty.

The results from the shift-error calculation are passed to the digital loop-filter. The user specifies the filter coefficients based on equation 16 and the software calculates the filtered output using equation 17. A separate routine allows the filter coefficients to change, depending on exposure location. For example, a larger bandwidth filter can be used for the first few lines of the field to rapidly correct the initial beam-position error. Once this error is corrected, the filter bandwidth can be narrowed to reduce the effect of estimation errors. In addition, fully exposed areas will have higher signal-to-noise ratios than sparsely patterned areas, and one might wish to adjust the filter coefficients based on pattern density.
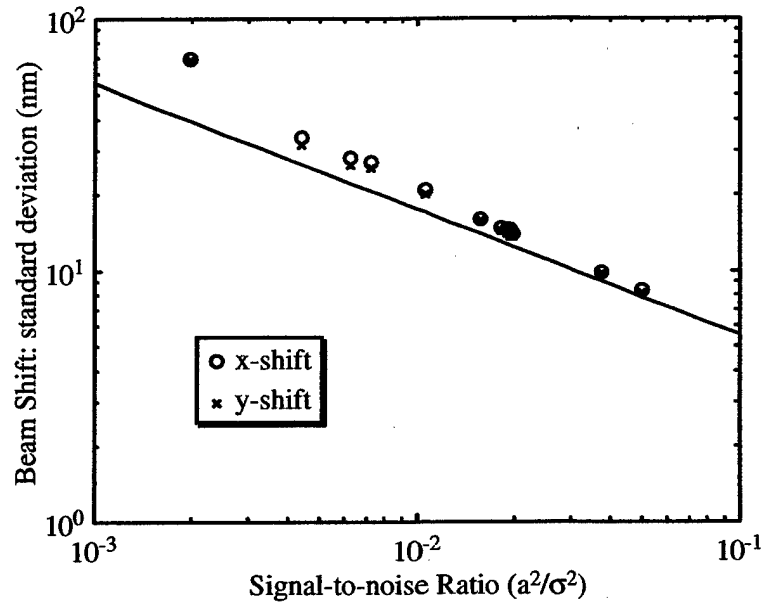
Figure 13: Standard deviation of shift error versus SNR measured over 10 μm $\times$ 10 μm regions of the deflection field. Also shown is the Cramer-Rao bound for phase-estimation of a sinusoid in white noise. Because the measured standard deviations track the lower bound, instead of reaching a minimum, we remain in a noise limited regime.

Currently, these adjustments must be preprogrammed by the user, but one can imagine an adaptive algorithm that monitors the signal-to-noise ratio and physical disturbances to continuously optimize the filter coefficients.

Next, we multiply the loop-filter output for each axis by a scaling factor to convert from beam displacement to the voltage required for deflection. These signals, x and y, are routed to the digital-to-analog converters whose output is summed electronically with the main deflection signal. For a 10kV exposure using a 100 μm field the beam deflects 300 nm/V. A voltage divider in line with the correction signal reduces this to 10 nm/V. The range of the DAC output, ($\pm$10V), covers corrections up to $\pm$100nm with 12-bit precision (LSB $\approx$ 0.05 nm). This range is sufficient for the errors found in a single field; however, the total drift between beam and stage over an entire exposure may be several hundred nanometers. Thus, after each field we add the cumulative correction to the Raith 150's shift correction which ranges up to $\pm$80μm . At the beginning of the next field the phase-locking system's correction is reset to zero.

7   Higher-order Distortion Correction

Several experiments with the Raith 150 revealed field-distortions that were not well corrected by first order (scale, rotation, and shift) parameters. Higher-order distortions must be minimized to achieve nanometer level pattern placement. Scanning over the fiducial grid is an excellent way to measure these errors, and one would hope to correct them using spatial-phase locking. Unfortunately, some of the distortions cause the beam position to vary too rapidly across the field for the SPL system to correct. As a result, we measure these distortions with respect to the fiducial grid, and then add the appropriate corrections to the feedback signal while exposing each field. The distortions need only be measured once per exposure, so the overhead time for this procedure is negligible.

It is not surprising that one can extend the field corrections with higher-order terms. To improve distortion in the Raith 150 system we implemented correction through third order with 10 terms per axis. We express the relationship between the desired and actual beam position as follows

$$x_B = a_0 + a_1 x_P + a_2 y_P + a_3 x_P y_P + a_4 x_P^2 + a_5 y_P^2$$
$$+ a_6 x_P^3 + a_7 y_P^3 + a_8 x_P^2 y_P + a_9 x_P y_P^2 \tag{21}$$
$$y_B = b_0 + b_1 x_P + b_2 y_P + b_3 x_P y_P + b_4 x_P^2 + b_5 y_P^2$$
$$+ b_6 x_P^3 + b_7 y_P^3 + b_8 x_P^2 y_P + b_9 x_P y_P^2 \tag{22}$$

where, once again, x_P is the ideal beam position and x_B is the actual beam position. One could estimate the coefficients in equations 21 and 22 by moving the stage to 10 different position and measuring the deviation of an image from it's expected position, but this is unnecessary with spatial-phase locking available. If one disables the feedback signals to the deflection system, and simply records the spatial-phase of the grid throughout the field, it is relatively straightforward to calculate the coefficients above.

In our implementation, we divide the deflection field into a 10 $\times$ 10 array of blocks. For a 100 μm field each of these blocks is 10 μm on a side, and if the address grid is 10 nm, each block contains 1000 $\times$ 1000 samples of the grid. Calculating the average beam-placement error in each of these blocks provides a map of the field distortion after only a single raster-scan. Figure 14(a) shows typical distortion with only first order corrections
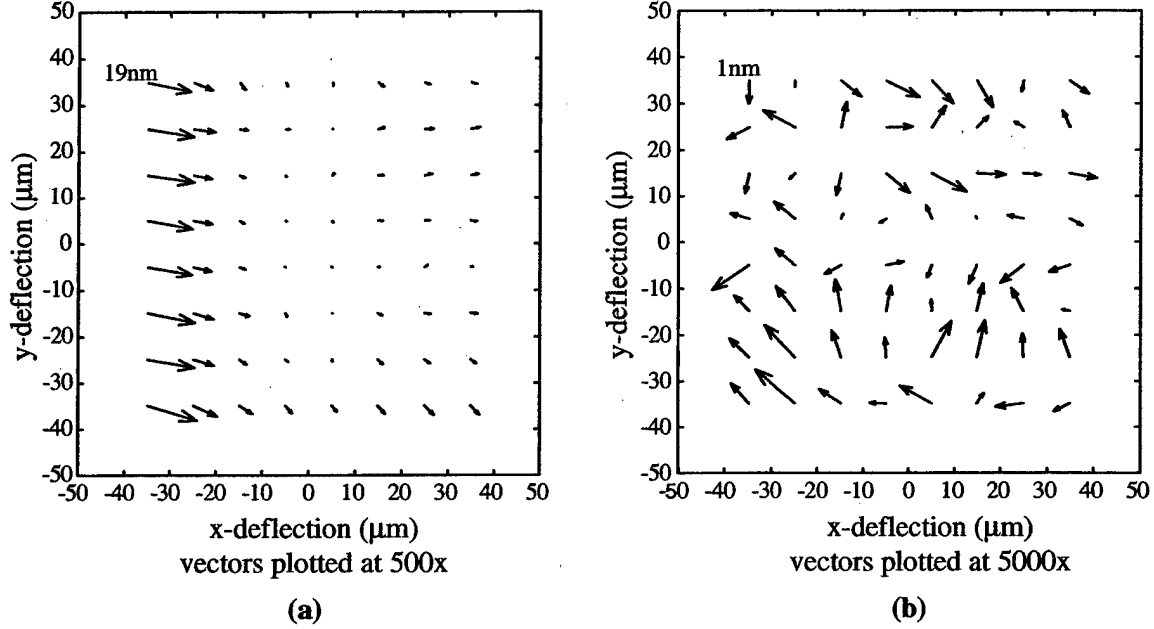
Figure 14: Field distortion maps: **(a)** First order correction only. **(b)** Correction through third order. Vectors indicate beam displacement from desired position for each point in the field. Note the difference in vector scaling between the two plots.

applied. The outermost distortion measurements are not shown in order to make the central region more clear. The extreme distortion at the left edge of the field is induced by the beam "fly back" between each exposed line. This error is reduced for boustrophedonic scanning, but different correction coefficients are required for left-to-right and right-to-left scanning. Distortion correction for both directions during boustrophedonic scanning is a straightforward and important future improvement.

Once a distortion map has been constructed one can calculate the correction coefficients with a least-squares solution to the following matrix equation.

$$
\begin{bmatrix} x_{B1} \\ x_{B2} \\ x_{B3} \\ \vdots \\ x_{B100} \end{bmatrix} = \begin{bmatrix} 1 & x_{P1} & y_{P1} & x_{P1}y_{P1} & x_{P1}^2 & y_{P1}^2 & x_{P1}^3 & y_{P1}^3 & x_{P1}^2 y_{P1} & x_{P1}y_{P1}^2 \\ 1 & x_{P2} & y_{P2} & x_{P2}y_{P2} & x_{P2}^2 & y_{P2}^2 & x_{P2}^3 & y_{P2}^3 & x_{P2}^2 y_{P2} & x_{P2}y_{P2}^2 \\ 1 & x_{P3} & y_{P3} & x_{P3}y_{P3} & x_{P3}^2 & y_{P3}^2 & x_{P3}^3 & y_{P3}^3 & x_{P3}^2 y_{P3} & x_{P3}y_{P3}^2 \\ & & & & & \vdots & & & & \\ 1 & x_{P100} & y_{P100} & x_{P100}y_{P100} & x_{P100}^2 & y_{P100}^2 & x_{P100}^3 & y_{P100}^3 & x_{P100}^2 y_{P100} & x_{P100}y_{P100}^2 \end{bmatrix} \begin{bmatrix} a_0 \\ a_1 \\ a_2 \\ a_3 \\ a_4 \\ a_5 \\ a_6 \\ a_7 \\ a_8 \\ a_9 \end{bmatrix}
$$

(23)

the coefficients for y-deflection correction can be calculated in the same way. These calculations are stored for the duration of the exposure and the appropriate corrections are added to the feedback signal as the beam scans over the field. Figure 14(b) shows the residual distortion after applying third order corrections. In the current implementation this correction is updated every 1000 samples; as a result, there are discretization errors at the left edge of the field not observable in the distortion map. Although the mean error is minimized for this region, the error changes too rapidly over 10 μm to be adequately corrected. For the experiments described in the next section, we used only a 60 μm $\times$ 60
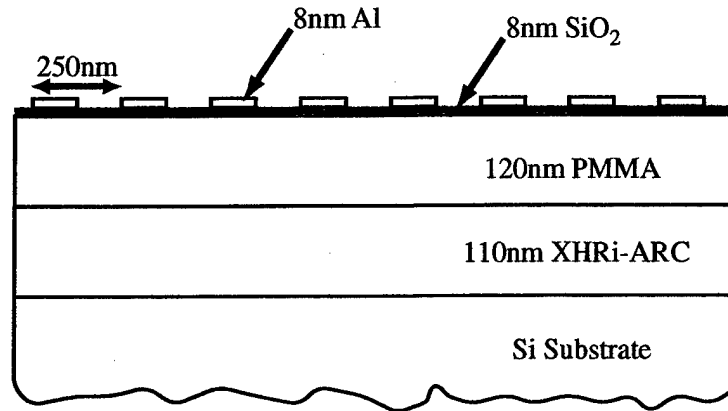
Figure 15: Resist and fiducial grid cross-section for real-time SPLEBL exposures. The anti-reflection coating (ARC) reduces the vertical standing wave in interference lithography, while PMMA serves as the e-beam resist. The SiO$_2$ layer prevents interaction of the positive IL resist with the PMMA, and the aluminum lattice forms the fiducial grid. The top two layers are largely electron transparent.

μm section of the field where the discretization error is below 1 nm.

8   Field-Stitching Experiments

We conducted field-stitching experiments to assess the effectiveness of real-time spatial-phase locking. In the absence of a dose-modulation scheme we were limited in the patterns that can be exposed. Nevertheless, we wrote arrays of 200-nm-period gratings with stitching errors below 1.3-nm (1-σ). In addition, every feature is placed with respect to the fiducial grid, so long-range pattern placement exhibits comparable precision.

An aluminum lattice served as the fiducial grid for the first set of real-time spatial-phase-locking experiments. It was formed on top of a 100-nm-thick layer of PMMA resist with the help of a 8-nm-thick SiO$_2$ interlayer and an underlying anti-reflection coating. The final layer structure is shown in figure 15. This particular structure was chosen to provide electrical continuity so that the grid could be biased for voltage contrast experiments. We did not use voltage contrast for initial spatial-phase-locking tests.

The grid itself was patterned with interference lithography in a positive resist (Sumitomo PFI-88) using a Lloyd's-mirror interferometer and a 325-nm wavelength HeCd laser. Two orthogonal exposures produced an array of posts in resist, and an 8-nm-thick aluminum layer was electron-beam evaporated onto to the sample. When the resist was removed only the aluminum lattice remained. Mirror non-flatness and spurious interference patterns limit the spatial-coherence of grids patterned with the Lloyd's-mirror inteferometer; therefore, one would not use such an interferometer for real masks or devices. However, the Lloyd's mirror provides rapid and convienient process development and the resulting grids are adequate for testing spatial-phase locking.

A sample with a 246-nm period grid was loaded into the Raith 150 system at an angle of

20

approximately -0.352 radians ($\approx -20.2^\circ$) with respect to the stage's x-axis. The deflection system can correct up to $\pm6^\circ$ of rotation, so mechanically setting the angle with a protractor was sufficient. Once loaded in the system, the laser-interferometer controlled stage was mapped to the grid coordinates by following a single grid line over several millimeters. Software was written to automate the stage movement and angle calculations. The stage was adjusted to move along axes rotated -0.352990 radians with respect to the grid. This angle was chosen because it provided an integral number of periods for k_{HI} and k_{LO} across a 99.624 μm field. As a result, one need not track accumulated phase shift from field to field. Field-to-field phase tracking can be implemented in future software revisions.

The Raith 150 system was configured for operation with a 10 keV beam energy and 172.9 pA beam current. Beam focus and stigmation were optimized by imaging 40-nm-diameter Au spheres applied to an unused portion of the sample from a colloidal suspension. Because we have not implemented a dose-modulation scheme in the Raith system, a test pattern was chosen where the beam remains on during almost the entire field exposure. This pattern, shown in figure 16, consists of 200-nm period vertical and horizontal gratings at each field boundary. Instead of exposing the grating lines themselves, we expose the entire surrounding area. After development, PMMA remains in regions where the beam was briefly turned off.

The Raith 150 system is installed close to a city street that is under construction, so the exposures were conducted at night when there is reduced vibration. Increasing the signal-to-noise ratio of the grid, and thus expanding the bandwidth of the feedback loop, would allow exposures in the presence of larger mechanical and acoustic disturbances.

The test pattern was isolated to a $60 \times 60\mu m$ region of the field where $-20\mu m \leq x \leq 40\mu m$ and $-30\mu m \leq y \leq 30\mu m$. Although the third-order distortion correction removes the mean displacement error over a larger area; these corrections are currently updated too infrequently. At the left edge of the field, when the beam is beginning its scan, errors within the 10 μm correction regions change by several nanometers. Thus, we decided to restrict the pattern to a region with sub-2-nm residual distortions. Patterning larger regions of the field will be possible after software revision for more frequent distortion correction.

The desired 10 keV dose, D, for such a pattern in PMMA is $70\mu C/cm^2$. With the given beam current, I_B, and a 9.962-nm (99.624 μm /10000) address grid, l, the dwell-time, dt, is

$$dt = \frac{l^2 D}{I_B} = 405 \text{ ns per pixel.} \tag{24}$$

This translates to a 2.469 MHz pixel clock. The patterns were exposed from left-to-right only, and 3 ms was allotted for beam settling after fly-back between lines. As a result, each field required 70 seconds to expose. This is not a throughput limit, even for the Raith system. Boustrophedonic scanning would reduce this exposure time to 40 seconds by eliminating most of the fly-back delay. In addition, one could use the full pattern generator speed, 10 MHz, with a higher beam current (available with only slight sacrifice of resolution) to obtain 10 second field exposures. These improvements would be beneficial for laboratory use, but the Raith system is fundamentally unsuited for high-throughput exposures.

We exposed 7×7 field arrays of the test pattern in figure 16 so that the gratings at the edge of one field align with those of the four adjacent fields. Figure 17 shows the overall pattern layout. Before starting the exposure we scanned the fiducial grid and calculated the first-order field correction coefficients (scale, rotation, and shift). These corrections were applied with the Raith field-correction hardware. Then we scanned the grid twice more
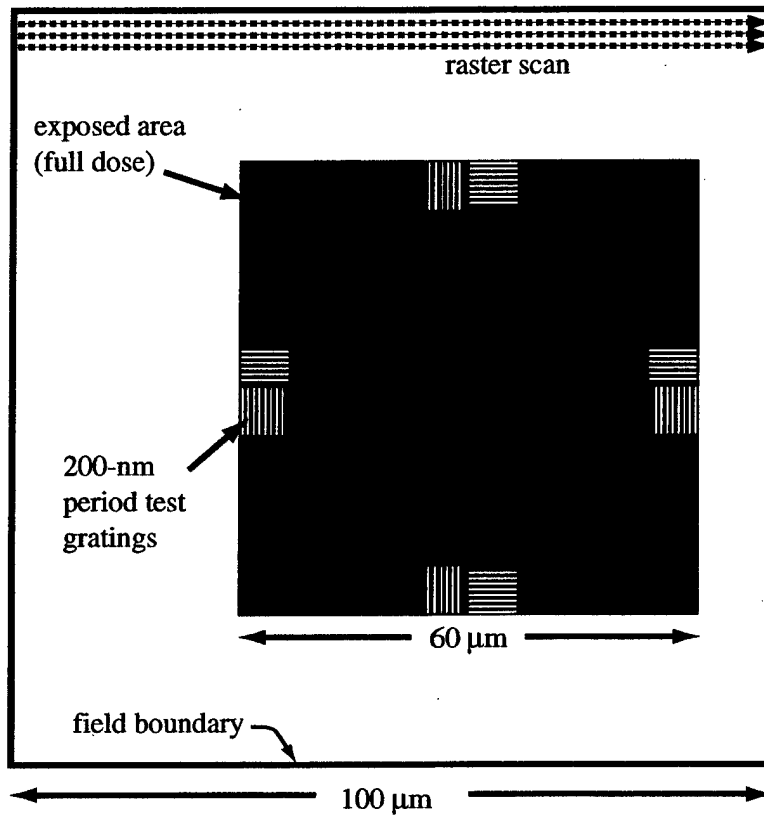
Figure 16: Field-stitching test pattern for real-time spatial-phase locking. The exposed pattern occupies a 60 μm $\times$ 60 μm square within the 100 μm field. The pattern contains horizontal and vertical 200-nm period gratings at the field boundaries for stitching measurements.

and calculated corrections through third order.[c] These revised corrections were applied simultaneously with the spatial-phase locking corrections.

Scanning the grid at the exposure dose showed that the standard deviation of the x- and y- shift estimates, over a $10\mu m \times 10\mu m$ region, was ≈ 14 nm. This is clearly in the noise-limited regime. Therefore, we set the loop filter coefficients to [0.0025 0.0025] for the numerator and [1 -1] for the denominator. This is approximately equivalent to an accumulator with a gain of 0.005. This should provide a noise component of $\sigma \approx 1$ nm for the feedback control signal. For the first 4 lines (40 nm) of the field the numerator coefficients were increased by a factor of 16. This allows the system to rapidly correct for the initial placement error present at the beginning of each field. Of course, this trade-off adds noise to the system for the first 4 lines in the field. Figure 18 plots the calculated system response for physical disturbances, $1/(1 + H_E H_F)$, for the initial and standard filter coefficients.

After exposing the field-stitching test patterns, we removed the aluminum grid and the SiO_2 interlayer using a buffered hydrofluoric acid solution ($\approx 10\%$ HF, Transene Co. Inc., Danvers, Ma.). We developed the PMMA in a solution of IPA and MiBK (2:1 by volume) for 60 seconds at 21.0 $^\circ$ C. The PMMA on ARC gratings were sputter coated with a gold-palladium alloy before measuring the stitching errors. Figure 19 shows the aligned gratings across the vertical and horizontal field boundaries. Beam-blanking oscillations are visible at the left edge of the horizontal grating lines.

The stitching precision was measured by comparing the spatial-phase of the grating across the field boundaries. Figure 20 shows histograms of the x- and y-stitching errors for vertical and horizontal boundaries. The mean errors, μ_{st}, ranged from -1.4 to 2.5 nm and the standard deviations, σ_{st} from 1.0 to 1.3 nm. Remeasuring the same grating pair 42 times yielded a standard deviation of 0.2 nm, so the measurement uncertainty is not significantly contributing to the observed standard deviations. In comparison, the manufacturer specifies stitching precision for the Raith 150 system as 40 nm, mean + 2 standard deviations. Our own evaluation of the system showed stitching errors between $\mu = -0.6$ nm, $\sigma = 6.2$ nm, and $\mu = -15.4$ nm, $\sigma = 9.1$ nm for a single exposure, depending on location in the field.

The Raith system does not guarantee global pattern placement, and the relative beam and stage position were found to drift by ≈ 6 nm per minute without spatial-phase locking. The system drifts faster until the sample and stage have thermally stabilized, and can drift more slowly under certain conditions. In contrast, all patterns exposed using spatial-phase locking are positioned with respect to the fiducial grid. As a result, we can estimate overall pattern-placement errors from relative stitching measurements. If the placement errors of features on opposite sides of the field boundary are uncorrelated, then the pattern placement precision, σ_{pp}, with respect to the grid is given by $\sigma_{pp} = \sigma_{st}/\sqrt{2} \leq 0.9$ nm. Without spatial-phase locking, stitching measurements are not a reliable measure of global placement precision. The slow drifts described above may produce small stitching errors

---

[c]For reference, the final correction values were

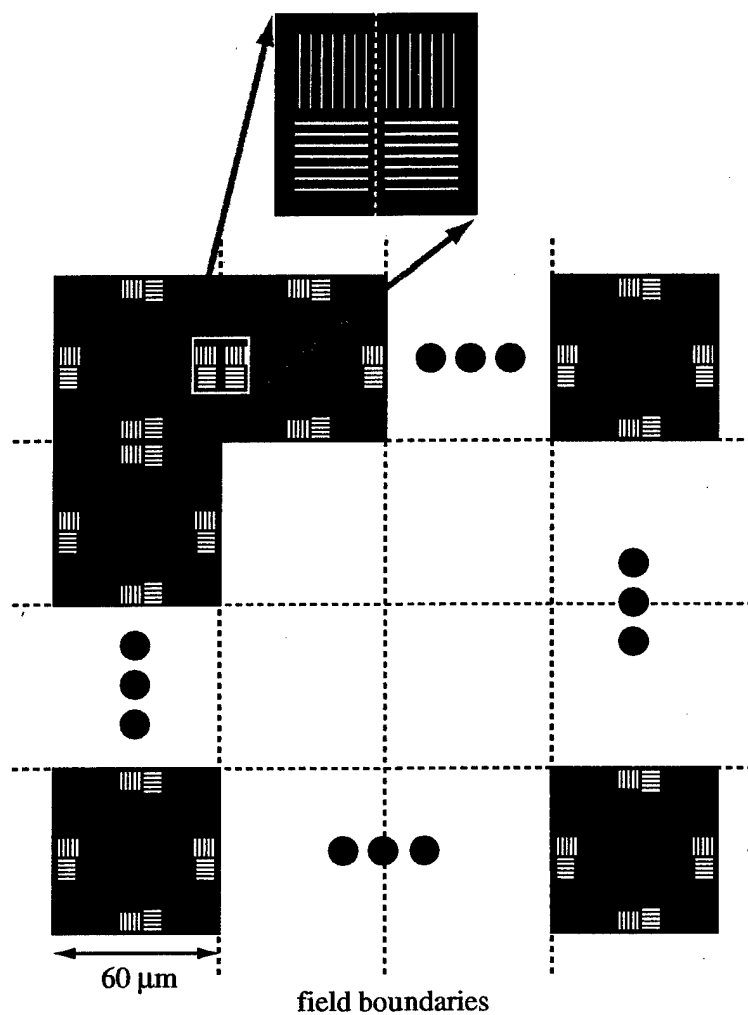|			
$a_0 = 8.95E - 6\mu m$	$a_5 = -3.0874E - 7\mu m^{-1}$	$b_0 = 4.22E - 3\mu m$	$b_5 = 2.4451E - 6\mu m^{-1}$
$a_1 = 9.9994E - 1$	$a_6 = 2.4776E - 7\mu m^{-2}$	$b_1 = -7.3047E - 6$	$b_6 = -3.405E - 8\mu m^{-2}$
$a_2 = 4.8335E - 5$	$a_7 = -1.1354E - 8\mu m^{-2}$	$b_2 = 9.9998E - 1$	$b_7 = -5.9220E - 9\mu m^{-2}$
$a_3 = -6.4194E - 7\mu m^{-1}$	$a_8 = -1.8704E - 8\mu m^{-2}$	$b_3 = -1.1284E - 6\mu m^{-1}$	$b_8 = -7.6222E - 9\mu m^{-2}$
$a_4 = -7.877E - 6\mu m^{-1}$	$a_9 = -5.751E - 9\mu m^{-2}$	$b_4 = 1.9806E - 6\mu m^{-1}$	$b_9 = 1.7146E - 8\mu m^{-2}$

Figure 17: Full pattern layout for field-stitching experiments. A 7 × 7 array of fields was exposed with the gratings aligned at each edge.
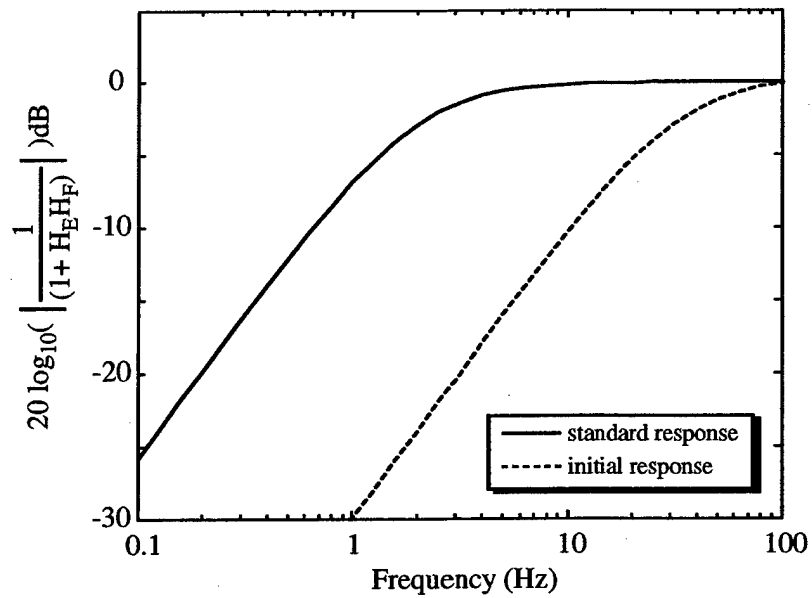
24

Figure 18: Calculated system response for physical distur-
bances for a 1000 point phase estimate. The dashed line
indicates the response for the first 4 lines in the field, and the
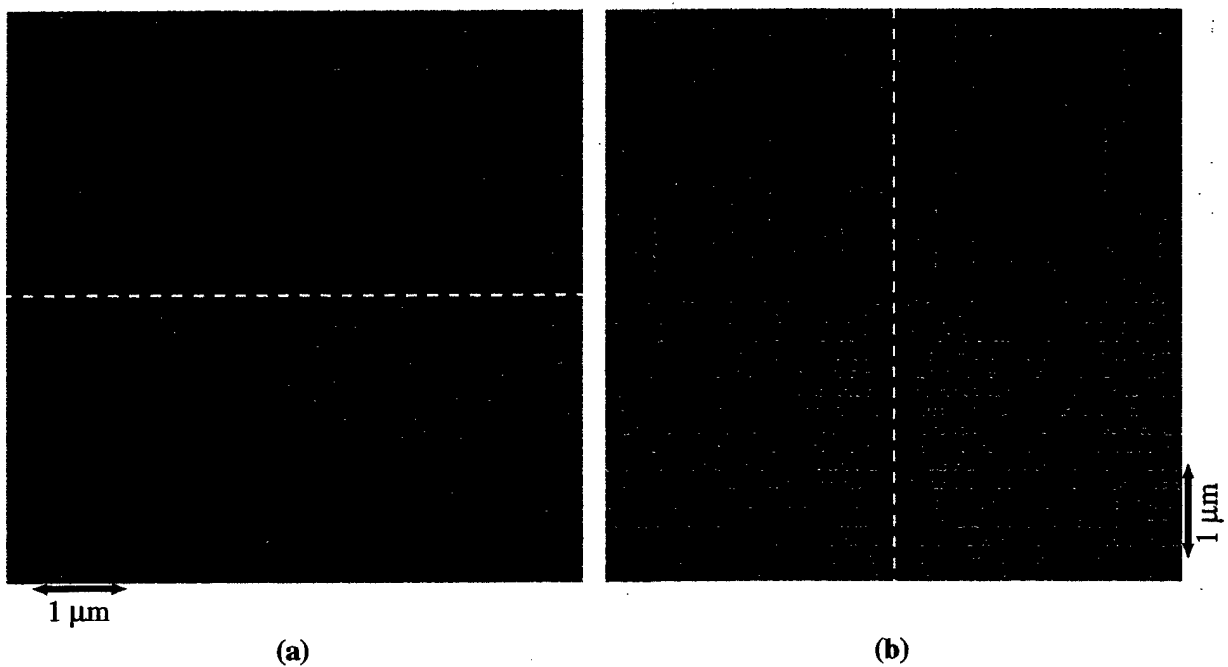solid line for the remainder of the field.

Figure 19: SEM of stitched gratings at the (a) horizontal and
(b) vertical field boundaries. The pattern intentionally con-
tains gaps between gratings so that the boundaries, denoted
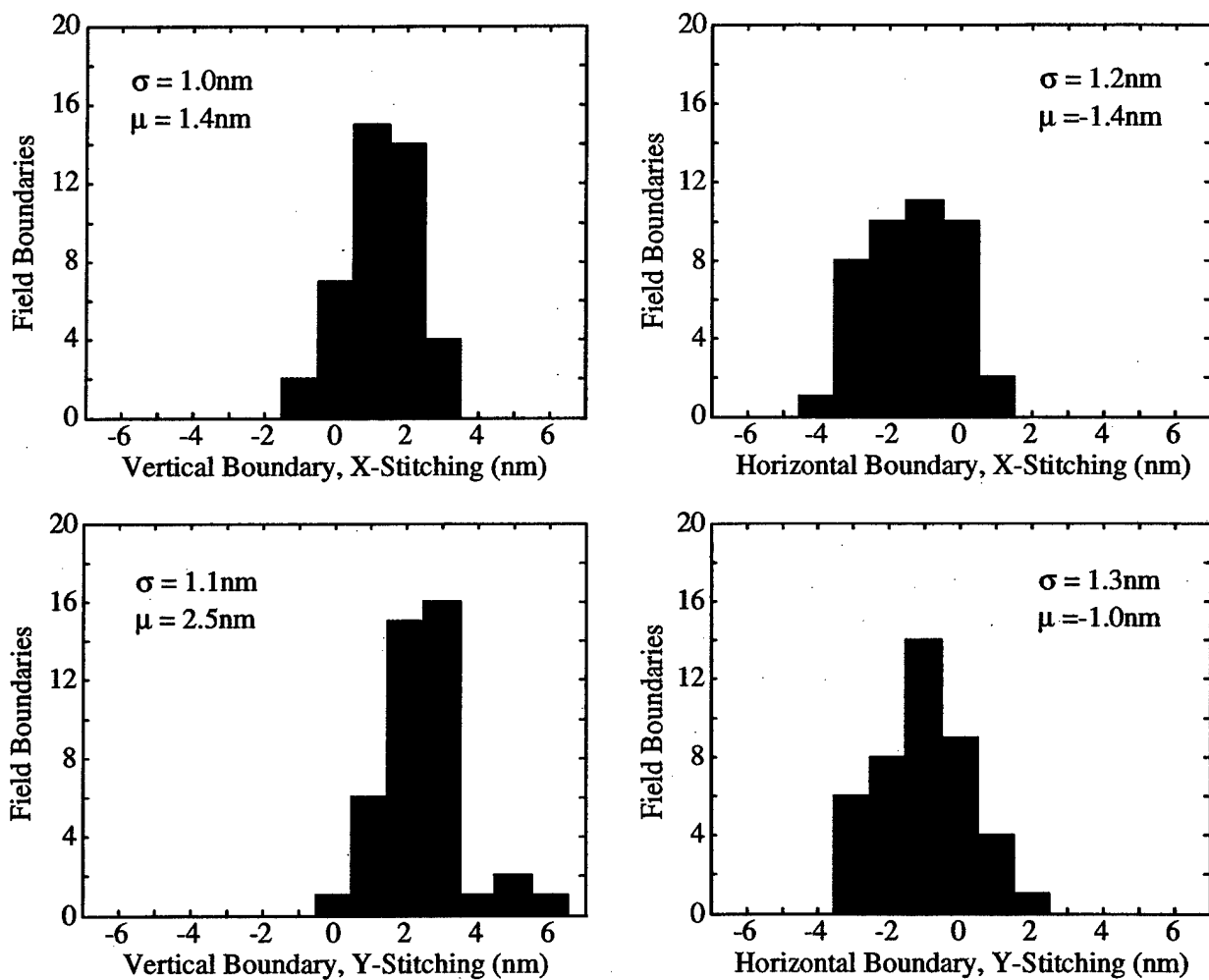by the dashed line, could be identified.

Figure 20: Stitching error histograms from real-time SPLEBL exposures. X- and Y-stitching measurements are shown for both vertical and horizontal boundaries, and the mean, μ, and standard deviation, σ, are included.

while a large global placement error accumulates

These results were obtained with the Raith 150, a converted scanning-electron microscope, in a standard laboratory environment. No special efforts were made to control temperature fluctuations, vibration, or electromagnetic interference beyond those present in the original electron microscope. The pattern-placement quality, though limited by the grid signal-to-noise ratio, confirms the importance of closed-loop control.

9 Remaining Engineering Issues for Commercial Implementation of SPLEBL

The research reported above, particularly the implementation of continuous-feedback, real-time SPLEBL, has clearly demonstrated the feasibility of 1-nm level absolute placement accuracy in SEBL. Such a capability is essential to the future of nanoelectronics and other elements of the nanotechnology revolution. However, a few engineering issues remain to be resolved before full commercial implementation of SPLEBL can be achieved. These issues are:

1. Development of a simple, low-cost means of putting down the fiducial grid that does not perturb the e-beam resist or adversely impact the resolution or linewidth control.

2. Improvement of the signal-to-noise ratio of the signal from the fiducial grid. This will enable the SPLEBL system to deal with higher frequency environmental disturbances, including mechanical vibration.

3. Development of a dose-modulating beam blanker so that phase locking can be fully continuous and applicable to patterns of arbitrary geometry.

4. Implementation of a hardware (dedicated chip) version of spatial-phase-locking so that higher writing speeds can be employed. (The current SPLEBL system is implemented in software on a dedicated general-purpose processor.)

5. Transfer of our SPLEBL technology to commercial vendors and to a manufacturer of low-cost, research-type e-beam systems (e.g. Raith).

6. Development of multi-level exposure capability with SPLEBL for mask-making and direct-write applications with critical overlay requirements.

A proposal has been submitted to DARPA whose objective is the resolution of these remaining issues.

10 List of Publications

1. J. T. Hastings, Feng Zhang, James Goodberlet, and Henry I. Smith, "Two-Dimensional Spatial-Phase-Locked Electron-Beam Lithography via sparse Sampling, ", *J. Vac. Sci. Technol. B* 18(6), 3268-3271, (2000).

2. Thomas E. Murphy, Mark K. Mondol and Henry I. Smith, "Characterization of field stitching in e-beam lithography using moir metrology", *J. Vac. Sci. Technol. B* 18(6), 3287-3291, (2000).

3. J.T. Hastings, F. Zhang, J.G. Goodberlet and H.I. Smith, "Improved Pattern-Placement Accuracy in E-Beam Lithography Via Sparse-Sample Spatial-Phase Locking", *Microelectronic Engineering* 53, 361-364, 2000.

4. T. E. Murphy, J. T. Hastings and Henry I. Smith, "Fabrication and Characterization of Narrow-Band Bragg-Reflection Filters in Silicon-on-Insulator Ridge Waveguides", *Journal of Lightwave Technology* 19(12) 1938-1942, (2001).

5. J. T. Hastings, J. G. Goodberlet and Henry I. Smith, "Performance of the Raith-150 Electron-Beam lithography System", *J. Vac. Sci. Technol. B* 19(6), 2499-2503 (2001).

6. A. A. Erchak, D. J. Ripin, S. Fan, P. Rakich, J.D. Joannopoulos, E. Ippen, G.S. Petrich and L. Kolodziejski, "Enhanced coupling to vertical radiation using a two-dimensional photonic crystal in a semiconductor light-emitting diode", *Appl. Phys. Let.* 78(5), 563-565 (2001).

7. H. I. Smith, "Low cost nanolithography with nanoaccuracy", *Physica E* 11, 104-109 (2001).

8. J.T. Hastings, M.H. Lim, J.G. Goodberlet and Henry Smith, "Optical Waveguides with Apodized Sidewall Gratings via spatial-phase-locked electron-beam lithography", *J. Vac. Sci. Technol. B* 20(6), 2753-2757, (2002).

9. John G. Hartley, Timothy R. Groves, Henry I. Smith, Mark K. Mondol, James G. Goodberlet, Mark L. Schattenburg, Juan Ferrera and Alexandr Bernshteyn, "Spatial-phase locking with shaped-beam lithography", *Review of Scientific Instruments* 74(3), 1377-1379, (2003).

10. F. J. Castano, C.A. Ross, C. Frandsen, A. Eilez, D. Gil, Henry I. Smith, M. Redjdal and F.B. Humphrey, "Metastable states in magnetic nanorings", *Physical Review B* 67, 184425, (2003).

11. J. T. Hastings, Feng Zhang, and Henry I. Smith, "Nanometer-Level Stitching in raster-Scanning E-Beam Lithography Using Spatial-Phase Locking", To be published in *J. Vac. Sci. and Technol. B* Nov./Dec. 2003.

12. F.J. Castano, C.A. Ross, A. Eilez, D. Gil and Henry I. Smith, "Magnetization reversal in lithographically defined elliptical-ring nanomagnets", Submitted to *Applied Physics Letters*, 2003.

13. F. Castano, A. Eilez, W. Jung, C. Frandsen, C. A. Ross, "Stability of Magnetic configurations in 160-520 nm diameter ferromagnetic rings", submitted *Phys. Rev. B*, (2003)

14. Minghao Qi, Steven G. Johnson, John D. Joannopoulos and Henry Smith, "Fabrication of three-dimensional photonic crystals with midgap wavelength at 1.55 um", Conference on Lasers and Electro-Optics", June 1-6, Baltimore, Maryland 2003.

15. Tymon Barwicz, Milos A. Popoviae, Peter T. Rakich, Michael R. Watts, Hermann Haus, Erich Ippen and Henry I. Smith, "Fabrication and analysis of add-drop filters based on microring resonators in SiN", submitted to OFC:04 (Optical Fiber Communication Conference) in Los Angeles CA from Feb 22-27, 2004.

11 Participating Scientific Personnel and Degrees Granted

1. Professor Henry I. Smith
2. Cynthia Caramana (Research Assistant)
3. Dr. A. A. Erchak (Ph.D. 2002)
4. Dr. Juan Ferrera (Ph.D. 2000)
5. Mark Finlayson (MS, 2000)
6. Dr. James Goodberlet
7. Dr. J. T. Hastings (Ph.D. 2003)
8. Daniel Kuepper (MS 2003)
9. Dr. Thomas Murphy (Ph.D. 2000)
10. Sander Smits (MS 2003)
11. Feng Zhang (Research Assistant)

Bibliography

[1] J. G. Hartley, T. R. Groves, H. I. Smith, M. K. Mondol, J. G. Goodberlet, M. L. Schattenburg, J. Ferrera, and A. Bernshteyn, "Spatial-phase locking with shaped-beam lithography," *Review of Scientific Instruments*, vol. 74, no. 3, pp. 1377–1379, 2003.

[2] J. Ferrera, "Nanometer-scale placement in electron-beam lithography," Ph.D. dissertation, Massachusetts Institute of Technology, June 2000.

[3] J. Ferrera, M. L. Schattenburg, and H. I. Smith, "Analysis of distortion in interferometric lithography," *J. Vac. Sci. Technol. B*, vol. 14, pp. 4009–4013, 1996.

[4] J. Ferrera, V. Boegli, E. H. Anderson, D. P. Kern, and H. I. Smith, "Spatial-phase-locked electron-beam lithography: Initial test results," *J. Vac. Sci. Technol. B*, vol. 11, no. 6, pp. 2342–2345, 1993.

[5] F. Zhang, Ph.D. dissertation, Massachusetts Institute of Technology, 2004, in preparation.

[6] J. Goodberlet, J. Carter, and H. I. Smith, "Scintillating global-fiducial grid for electron-beam lithography," *J. Vac. Sci. Technol. B*, vol. 16, no. 6, pp. 3672–3675, 1998.

[7] M. A. Finlayson, "Scintillator for spatial-phase-locked e-beam lithography," Master's thesis, Massachusetts Institute of Technology, June 2001.

[8] H. I. Smith, S. D. Hector, M. K. Schattenburg, and E. H. Anderson, "A new approach to high fidelity e-beam and ion-beam lithography based on an *in situ* global-fiducial grid," *J. Vac. Sci. Technol. B*, vol. 9, no. 6, pp. 2992–2995, 1991.

[9] J. Goodberlet, J. Ferrera, and H. I. Smith, "Spatial-phase-locked electron-beam lithography with a delay-locked loop," *J. Vac. Sci. Technol. B*, vol. 15, no. 6, pp. 2293–2297, 1997.

[10] J. Goodberlet, S. Silverman, J. Ferrera, M. Mondol, M. Schattenburg, and H. I. Smith, "A one-dimensional demonstration of spatial-phase-locked electron-beam lithography," *Microelectronic Engineering*, vol. 35, pp. 473–476, 1997.

[11] J. G. Goodberlet, J. T. Hastings, and H. I. Smith, "Performance of the raith 150 e-beam lithography system," *J. Vac. Sci. Technol. B*, vol. 19, no. 6, pp. 2499–2503, 2001.

[12] R. A. Forber, Z. W. Chen, S. Mrowka, C. G. Gaeta, K. Cassidy, H. I. Smith, and I. C. E. Turcu, "Collimated point-source X-ray nanolithography," *J. Vac. Sci. Technol. B*, vol. 20(6), pp. 2984–2990, Nov/Dec. 2002.

[13] J. O. Choi, A. I. Akinwande, and H. I. Smith, "100 nm gate hole openings for low voltage driving field emission display applications," *J. Vac. Sci. Technol. B*, vol. 19(3), pp. 900–903, 2001.

[14] J. T. Hastings, F. Zhang, M. A. Finlayson, J. G. Goodberlet, and H. I. Smith, "Two-dimensional spatial-phase-locked electron-beam lithography via sparse sampling," *J. Vac. Sci. Technol. B*, vol. 18, no. 6, pp. 3268–3271, 2000.

[15] J. G. Goodberlet, J. Ferrera, M. Farhoud, V. Z. Chan, and H. I. Smith, "Extending spatial-phase-locked electron-beam lithography to two dimensions," *Jpn. J. Appl. Phys.*, vol. 36, no. 12B, pp. 7557–7559, 1997.

[16] J. Goodberlet, J. Ferrera, and H. I. Smith, "An analogue delay-locked loop for spatial-phase locking," *Electronics Letters*, vol. 33(15), pp. 1269–1270, 1997.

[17] X. Zhuang, D. Conkerton, A. Lal, M. Feldman, T. O'Reilly, and H. I. Smith, "Adaptive membrane masks," submitted to the 2003 International Conference on Electron, Ion and Photon Beam Technology and Nanofabrication.